Numerical Investigations on Dynamic Stall Characteristics of a Finite Wing

*JING Simeng, CAO Chenkai, GAO Yuan, ZHAO Qijun, ZHAO Guoqing**

National Key Laboratory of Helicopter Aeromechanics, Nanjing University of Aeronautics and Astronautics, Nanjing 210016, P. R. China

(Received 10 January 2024; revised 28 February 2024; accepted 21 June 2024)

Abstract: The paper examines the dynamic stall characteristics of a finite wing with an aspect ratio of eight in order to explore the 3D effects on flow topology, aerodynamic characteristics, and pitching damping. Firstly, CFD methods are developed to calculate the aerodynamic characteristics of wings. The URANS equations are solved using a finite volume method, and the two-equation k-ω shear stress transport (SST) turbulence model is employed to account for viscosity effects. Secondly, the CFD methods are used to simulate the aerodynamic characteristics of both a static, rectangular wing and a pitching, tapered wing to verify their effectiveness and accuracy. The numerical results show good agreement with experimental data. Subsequently, the static and dynamic characteristics of the finite wing are computed and discussed. The results reveal significant 3D flow structures during both static and dynamic stalls, including wing tip vortices, arch vortices, Ω-type vortices, and ring vortices. These phenomena lead to differences in the aerodynamic characteristics of the finite wing compared with a 2D airfoil. Specifically, the finite wing has a smaller lift slope during attached-flow stages, higher stall angles, and more gradual stall behavior. Flow separation initially occurs in the middle spanwise section and gradually spreads to both ends. Regarding aerodynamic damping, the inboard sections mainly generate unstable loading. Furthermore, sections experiencing light stall have a higher tendency to produce negative damping compared with sections experiencing deep dynamic stall.

Key words: finite wing; dynamic stall; aerodynamic damping; 3D effects

CLC number: V212.4 **Document code:** A **Article ID:** 1005-1120(2024)04-0444-14

0 Introduction

In the field of helicopter rotor aerodynamics, dynamic stall has achieved extensive attention due to its detrimental impacts. This phenomenon occurs when the helicopter experiences high-speed forward flight or high-load maneuvers[1]. Dynamic stall results in a rapid increase in torque and vibration, leading to a loss of thrust and posing a threat to the overall safety of the helicopter. Consequently, dynamic stall imposes limitations on the maximum flight speed that a helicopter can attain.

Up to now, the majority of investigations on dynamic stall have been conducted on 2D airfoils. In the deep dynamic stall regime, the dynamic stall vortex (DSV) plays a significant role over a wide range of Reynolds numbers ($10^4 \leqslant Re \leqslant 10^6$)[2]. Dynamic stall is influenced by various factors, including compressibility[3-9], Reynolds number[6,10-12], reduced frequency[6,13], the maximum angle of attack (AoA), and airfoil geometry[14-16]. While there has been notable progress in understanding the sequence of events and mechanism of dynamic stall on 2D airfoils, it is important to recognize that dynamic stall is actually a 3D flow phenomenon. Studying the dynamic stall characteristics of finite wings can enhance the understanding of the 3D dynamic stall and aid in the design of aircraft wings and rotorcraft blades. Hence, several research has been conducted on the dynamic stall of finite wings.

*Corresponding author, E-mail address: zgq198495@nuaa.edu.cn.

How to cite this article: JING Simeng, CAO Chenkai, GAO Yuan, et al. Numerical investigations on dynamic stall characteristics of a finite wing[J]. Transactions of Nanjing University of Aeronautics and Astronautics, 2024, 41(4): 444-457.

http://dx.doi.org/10.16356/j.1005-1120.2024.04.003

A series of experimental measurements have been conducted on finite wings. Ref.[17] measured the pressure distribution over a NACA 0015 wing at different reduced frequencies and pitching angles. The experiments provided valuable data on the unsteady aerodynamic loads. Ref.[18] conducted experiments on a NACA 0015 wing using dye flow visualization and surface pressure measurements. They found that the initially 2D DSV experienced 3D deformation and transformed into an arch-type vortex during the ramping motion. Ref.[19] conducted pressure measurements on a pitching NACA 0012 wing. The experimental data were utilized to detect the onset and evolution of DSV and to extend the ONERA semiempirical theoretical model to 3D flow. Ref.[20] examined the dynamic stall of a NACA 0015 wing by utilizing surface pressure measurements. It was found that the DSV initially formed near the midspan and its convection characterized highly 3D features with the pressure response indicative of the signature of an Ω-type vortex. Refs.[21-22] measured the boundary layer velocity profiles of a pitching tapered wing by employing an embedded laser Doppler velocimetry (LDV) technique. Ref.[23] conducted tests on the dynamic stall characteristics of an OA209 wing by employing pressure transducers, LDV, and particle image velocimetry (PIV) techniques. Various factors, including Reynolds effects, swept effects, dynamic stall onset, and 3D effects, were analyzed. The findings revealed that the flow separation, which originated from the inner part of the wing and extended towards the wing tip, was impeded by the presence of wing tip vortex (TV). Ref.[24] conducted experiments on a pitching parabolic-tip wing. The analysis of surface pressure and flow topology revealed that complete flow separation initiated inboard of the wing. Additionally, the flow separation at the wing tip resembled more of a light stall due to a significant reduction in the effective AoA.

Apart from the experimental research, computational studies have been performed on 3D dynamic stall. Ref.[25] used the URANS method to simulate the aerodynamic characteristics of a NACA 0015 wing and analyzed the effects of subiterations, time step, and grid density on the accuracy of the computed solutions. Ref.[26] conducted a numerical analysis on the laminar flow characteristics of both a 2D NACA 0012 airfoil and a 3D wing. The results showed that the initiation of leading edge vortices was similar for both the 2D and 3D cases. As the pitch angle increased, the flow features of the center plane of 3D wing and the 2D airfoil diverged due to the onset of 3D effects. Refs.[27-28] carried out simulations and analyses on different test cases[18, 20-21]. In the dynamic stall stages, researchers noticed the occurrence of a Π-Ω vortex system, which arises from the interaction between the DSV and TV. Ref.[29] utilized the detached eddy simulation (DES) method to simulate the dynamic stall characteristics of a NACA 0015 wing. The study investigated the behavior of the TV and observed its breakup at the end of the upstroke. Refs.[30-32] conducted numerical research on the dynamic stall characteristics of the tested OA209 wing[23]. They extensively compared the numerical and experimental results. Furthermore, they discovered that the Ω-type vortex evolves through the interaction of the TV. Ref.[33] conducted numerical investigations on a pitching DSA-9A wing using the URANS method. The reduced frequency was found to significantly influence the flow topology of the wing. At low frequencies, flow separation was initiated at the wing tip and propagated towards the root. Whereas, at high frequencies, a leading-edge vortex formed at a more inboard section before expanding in both directions. Refs.[2, 34] conducted a study on the evolution of unsteady flow structure and the impact of sweep on dynamic stall of a finite wing using the high resolution implicit large eddy simulation (ILES) method. It was observed that during the dynamic stall process, the DSV evolved into an arch-type structure which was shed following its transformation into a ring vortex. In the case of the rectangular wing, there was a single, larger arch vortex centered about the midspan. However, for the swept wings, arch vortices formed on each side of the wing at a spanwise station that moved increasingly outboard with greater sweep. Ref.[35] conducted a simulation to investigate the dynamic stall character-

istics of a finite wing. The findings revealed that the presence of the TV and spanwise flow mitigated the dynamic stall near the wing's two ends.

Previous studies have explored the dynamic stall of finite wings through experimental and numerical approaches. The majority has been conducted at low Mach numbers and medium Reynolds numbers. Moreover, there is a lack of investigation into the aerodynamic damping of 3D dynamic stall cases. Therefore, this study aims to investigate the dynamic stall and examine the pitching damping of a finite wing at higher Mach and Reynolds numbers.

In this research, the URANS method is used to simulate the aerodynamic characteristics of finite wings. The effectiveness and accuracy of the CFD methods are validated by comparing the numerical and experimental results. The study then focuses on simulating the dynamic stall characteristics of a pitching wing. By analyzing the flow structures, the evolution of the DSV is discussed. Additionally, the 3D effects on the aerodynamic characteristics of the finite wing are analyzed by comparing them with those of a 2D airfoil. Furthermore, the aerodynamic damping of the pitching airfoil, 3D wing, and wing sections are examined. Finally, the analysis leads to several meaningful conclusions.

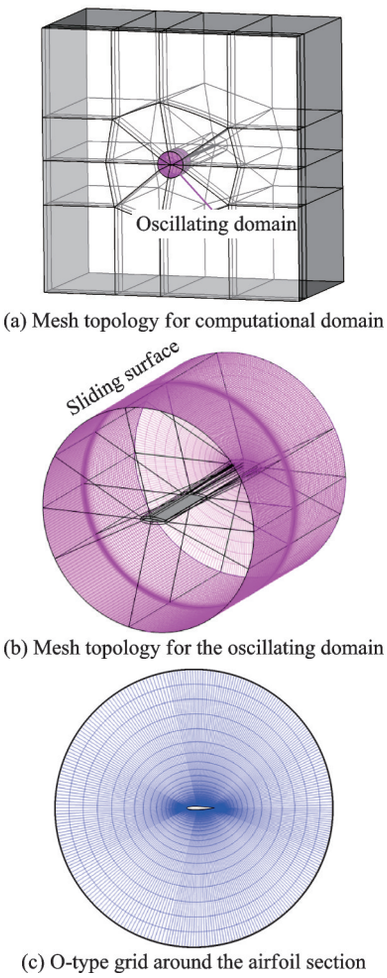

(a) Mesh topology for computational domain

(b) Mesh topology for the oscillating domain

(c) O-type grid around the airfoil section

Fig.1 Mesh topology for the finite wing

1 Numerical Methods

1.1 Sliding mesh

The sliding and structural mesh is adopted in the research work. Fig.1(a) shows the overall mesh topology for the computational domain. The computational domain is a rectangular cuboid, with its outer boundary located at a distance of 50 times the chord length from the wing surface. The computational domain is divided into an oscillating domain surrounding the finite wing and a static background domain. The mesh topology for the oscillating domain and the grid distribution of airfoil section are shown in Figs.1(b, c), respectively. The sliding surface is located at a distance of 5 times the chord length from the wing surface. The wing surface has 316 grid points in the chordwise direction and 81 grid points in the spanwise direction with a leading edge spacing equal to 0.1% of the chord length c and a trailing edge spacing equal to $0.4\%c$. In the wingtip area, the grid has a spacing of $0.1\%c$ in the spanwise direction. There are 29 grid points in the boundary layer, and the initial wall spacing in the normal direction is equal to $6.5\times10^{-6}c$ for a dimensionless wall distance $y^+<1$. The total number of grid points in the oscillating and background domains are approximately 4.5 million and 4.6 million, respectively.

1.2 Governing equations and solutions

The RANS equations are solved by the in-house CLORNS code[36] to simulate the aerodynamic characteristics of the finite wing. The governing equations are

$$\frac{\partial}{\partial t}\int_{\Omega}\boldsymbol{W}\mathrm{d}\Omega+\oint_{\partial\Omega}(\boldsymbol{F}_{\mathrm{c}}-\boldsymbol{F}_{\mathrm{v}})\cdot\boldsymbol{n}\mathrm{d}S=0 \tag{1}$$

where $\partial\Omega$ denotes the boundary of a control volume

Ω; and $\boldsymbol{n}$ the unit normal vector of the surface element dS. $\boldsymbol{W}$, $\boldsymbol{F}_c$, and $\boldsymbol{F}_v$ are the vectors of conserved variables, convective fluxes, and viscous fluxes, respectively.

The k-ω shear stress transport (SST) turbulence model is adopted to account for the effects of turbulence. The governing equations of the SST model are

$$\frac{\partial(\rho k)}{\partial t}+\nabla\cdot(\rho \boldsymbol{V}k)=P_k-\rho C_\mu k\omega+\nabla\cdot\left[(\mu_l+\sigma_k\mu_t)\nabla k\right] \tag{2}$$

$$\frac{\partial(\rho\omega)}{\partial t}+\nabla\cdot(\rho \boldsymbol{V}\omega)=\frac{\alpha\rho}{\mu_t}P_k-\beta\rho\omega^2+\nabla\cdot\left[(\mu_l+\sigma_\omega\mu_t)\nabla\omega\right]+2(1-F_1)\rho\sigma_{\omega2}\frac{\nabla k\cdot\nabla\omega}{\omega} \tag{3}$$

where k and ω are the turbulent kinetic energy and its specific dissipation rate, respectively. F_1 is the blending function. The first three terms on the right sides of equal sign in Eqs.(2,3) represent eddy-viscosity production, dissipation, and conservative diffusion, respectively. The last term in Eq.(3) is a cross derivative. The production term is

$$P_k=\min\left(\mu_t S^2, 10C_\mu\rho k\omega\right) \tag{4}$$

where μ_t is the turbulent viscosity, S the invariant measure of the strain rate, ρ the air density, and C_μ a constant.

The finite volume method is used to solve the governing equations, with time integration performed using the second order implicit backwards difference method scheme with LU-SGS method. The dual-time-stepping subiterations use a local time step, and the simulation employs 50 subiterations, which ensures that the residual decreases by 1—3 orders in the magnitude. The 3rd-order Roe-MUSCL spatial scheme is used to calculate the convective fluxes.

1.3 Validations

1.3.1 Static cases

Pressure measurements are performed on a finite wing in the low speed wind tunnel in National Key Laboratory of Helicopter Aeromechanics of Nanjing University of Aeronautics and Astronautics. The test model is a straight wing with a chord length of 0.2 m and a span of 0.5 m, using SC1095 airfoil section. One end of the model is fixed to the test support. The model is made from high-strength aluminum alloy and is internally equipped with a metal skeleton. There are a total of 48 pressure tap orifices located at three spanwise positions on the surface, namely, 0.15, 0.25, and 0.4 m away from the wing root, respectively. The orifices are symmetrically distributed over the upper and lower surfaces at positions of 0.025, 0.05, 0.1, 0.2, 0.4, 0.6, 0.8, and 0.85, expressed as a percentage of the chord length from the leading edge. A multi-channel pressure scanner and a digital data acquisition system are used to collect the pressure distribution over the three spanwise sections. Fig.2 displays photos of the test model, the wing tunnel test section, and the measurement equipment. The measured pressure coefficients are used to validate the numerical methods.

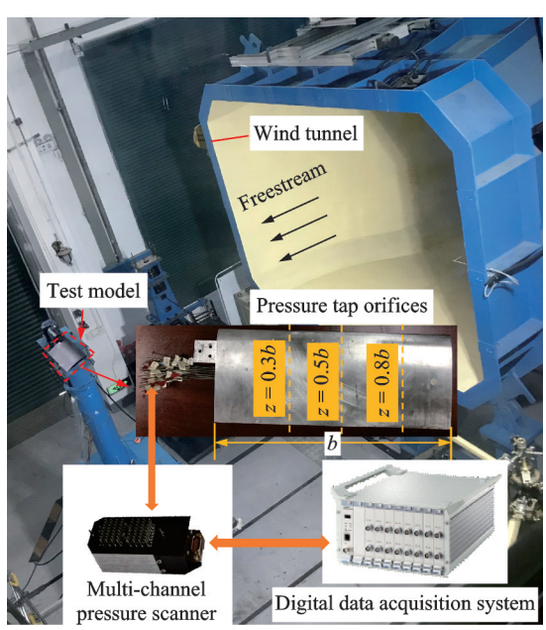

Fig.2 Photos of test model, wing tunnel test section, and measurement equipment

Fig.3 and Fig.4 compare the experimental and numerical pressure coefficients of three spanwise sections of the finite wing at two AoAs. At an AoA of 14°, the flow remains attached to the wing surface, and the numerical results show good agreement with the experimental data. At an AoA of 16°, the experimental pressure coefficient C_p indicates that the flow still remains attached over the wing

surface. The numerical method predicts an earlier flow separation for the middle section. Overall, the CFD method provides acceptable results.

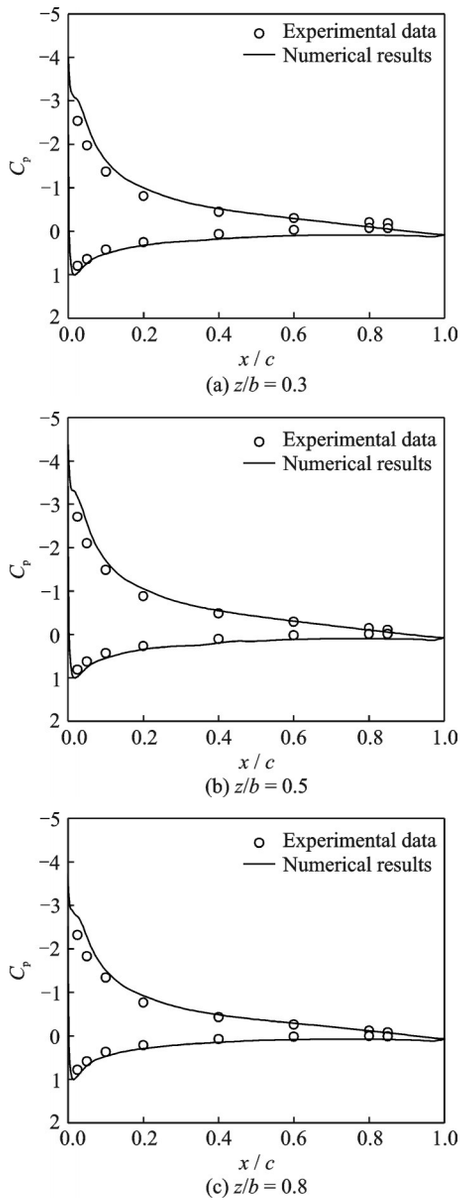

Fig.3 Pressure coefficients of the finite wing at u_∞ = 30 m/s, $\alpha = 14^\circ$

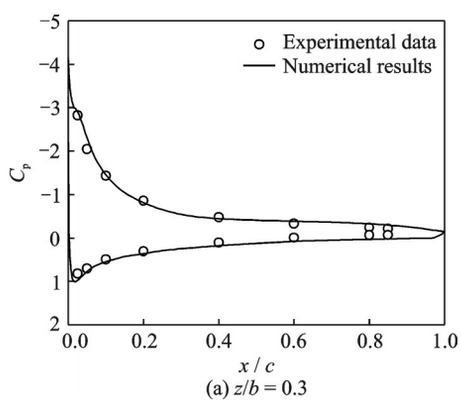

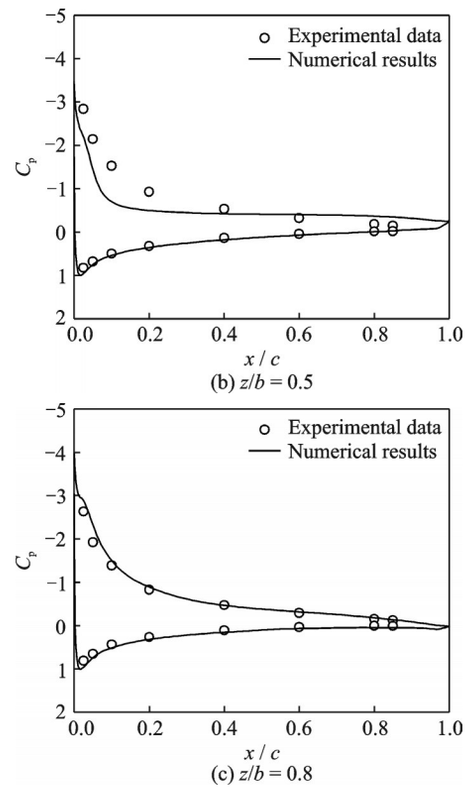

Fig.4 Pressure coefficients of the finite wing at u_∞ = 30 m/s, $\alpha = 16^\circ$

1.3.2 Dynamic cases

Refs.[21-22] performed measurements on the velocity profiles of the boundary layer for an oscillating, tapered wing. The schematic diagram of the experimental model is shown in Fig.5. The wing has a span of 0.428 m, the wing root has a chord length of 0.24 m, and the wing tip has a chord length of 0.06 m. At the leading and trailing edges, the swept angles are 84° and 72.5°, respectively.

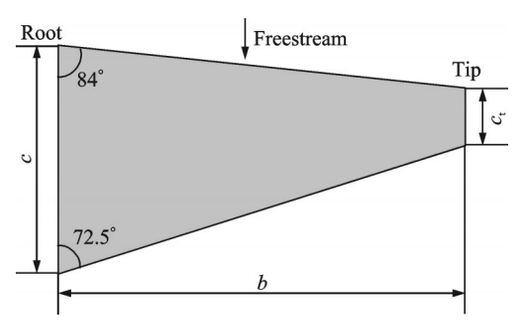

Fig.5 Schematic diagram of the experimental model

The aerodynamic characteristics of the tapered wing at a freestream velocity of 62.5 m/s are computed. In the case, the wing oscillates with a mean angle of 18°, an amplitude of 6°, and a reduced frequency of 0.048. Fig.6 shows the comparisons of u-

velocity profiles at four phase angles, where the arrows " ↑ "and " ↓ " represent upstroke and downstroke circle, respectively. The u-velocity profiles at phase angles of 0° and 270° indicate an attached flow. In contrast, the velocity profiles at 90° and 180° reveal a separated flow. Overall, the numerical results are found to be in good agreements with the experimental results, indicating the effectiveness and accuracy of the numerical methods.

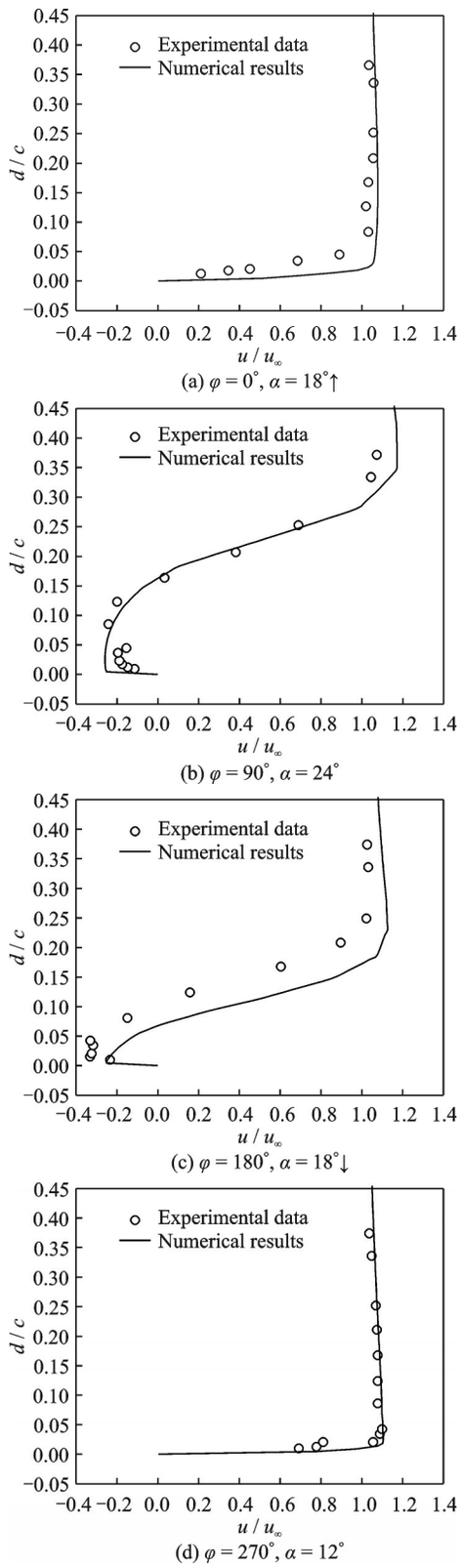

Fig.6 Comparisons of numerical and experimental results for u-velocity profiles at $z = 0.5b$ and $x = 0.6c$

2 Results and Discussion

2.1 Computational model

Computations and analyses are performed for a NACA0012 wing with a chord length of 0.61 m, a span of 4.88 m and zero twist, shown in Fig.7. The wing has a high aspect ratio $AR = b/c = 8$. Both static and dynamic characteristics of the wing are simulated and analyzed at a Mach number of 0.283. The Reynolds number based on the chord length is 3.9×10^6.

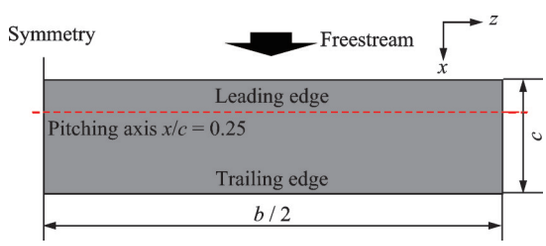

Fig.7 Pitching wing configuration

2.2 Static characteristics

The static, aerodynamic characteristics of the wing are computed at a Mach number of 0.283. The lift, drag and pitching moment coefficients (C_l, C_d, C_m) are shown in Fig.8. The experimental data at

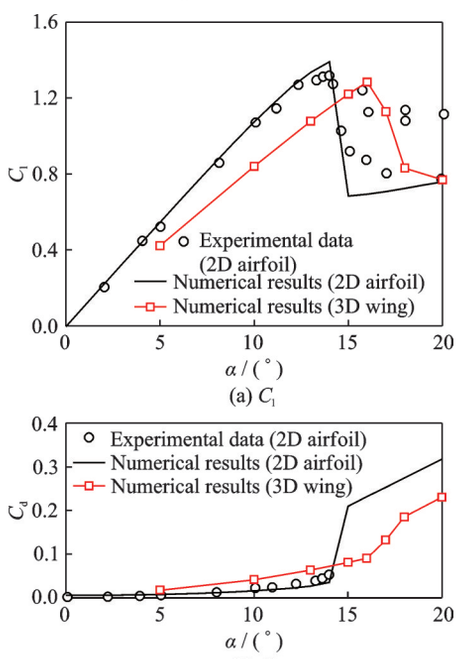

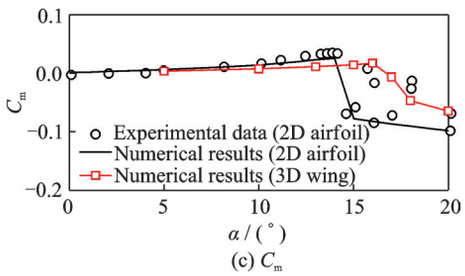

Fig.8 Comparisons of force coefficients between 2D airfoil and 3D wing

$Ma = 0.3$[37] and the numerical results at $Ma = 0.283$ of the NACA 0012 airfoil are also included in Fig.8. At low AoAs, the wing generates smaller lift, higher drag and slightly higher nose-down pitching moment compared to the 2D airfoil. Additionally, the wing has a smaller lift slope than the 2D airfoil. However, the wing stalls at a higher AoA than the 2D airfoil and the changes in aerodynamic force after stall are more gradual. These phenomena can be attributed to the influence of 3D flow on the finite wing.

Fig.9 displays the iso-surface of Q colored by pressure coefficient for the finite wing at different AoAs. At α=10° and 15°, flow is attached over the wing surface except that two tip vortices form near the two ends of the wing. The tip vortices induce

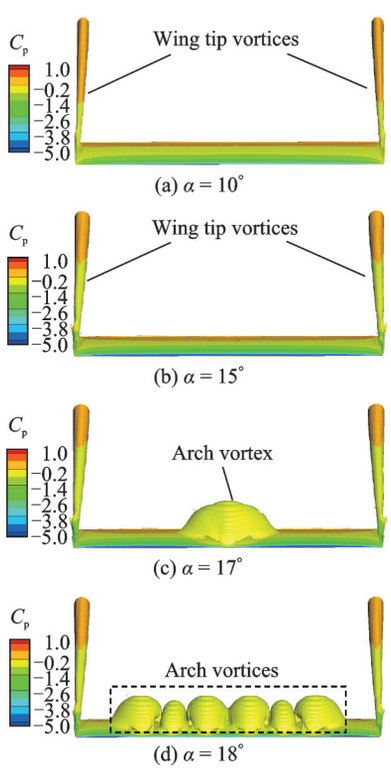

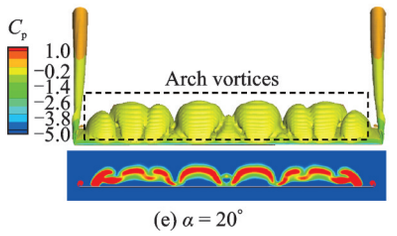

Fig.9 Iso-surface of Q colored by pressure coefficient for the finite wing at different angles

downwash flow over the upper surface of the wing, leading to a reduction in the effective angle and lift. As the AoA increases, the strength of the tip vortices intensifies, resulting in a higher loss of lift at larger angles. This phenomenon predominantly accounts for the decreased lift slope observed in finite wings. The 2D airfoil experiences a dramatic drop in lift and an abrupt increase in drag and nose-down pitching moment (shown in Fig.8), revealing that the airfoil encounters significant flow separation and stall at an AoA of 15°. The downwash flow induced by the wing tip vortices reduces the effective angle of the wing, thus delaying the occurrence of stall. As the AoA is increased to 17°, an arch vortex forms near the middle section of the wing span, indicating that flow separation initially occurs in the middle section. With further increase in AoA, the separated region extends to both wing tips and additional arch vortices generate over the upper surface, as shown in Figs.9(d,e). The extension of separated flow from middle section to wing tip results in the gradual variation in aerodynamic force of the finite wing.

Fig.10 presents a schematic diagram illustrating the positions of four spanwise sections of the wing. In Fig.11, a comparisons of pressure coefficients between the wing sections and 2D airfoil is

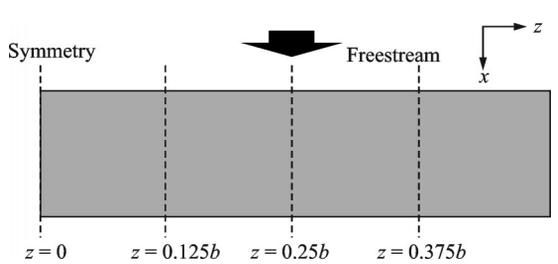

Fig.10 Schematic diagram of the positions of spanwise sections

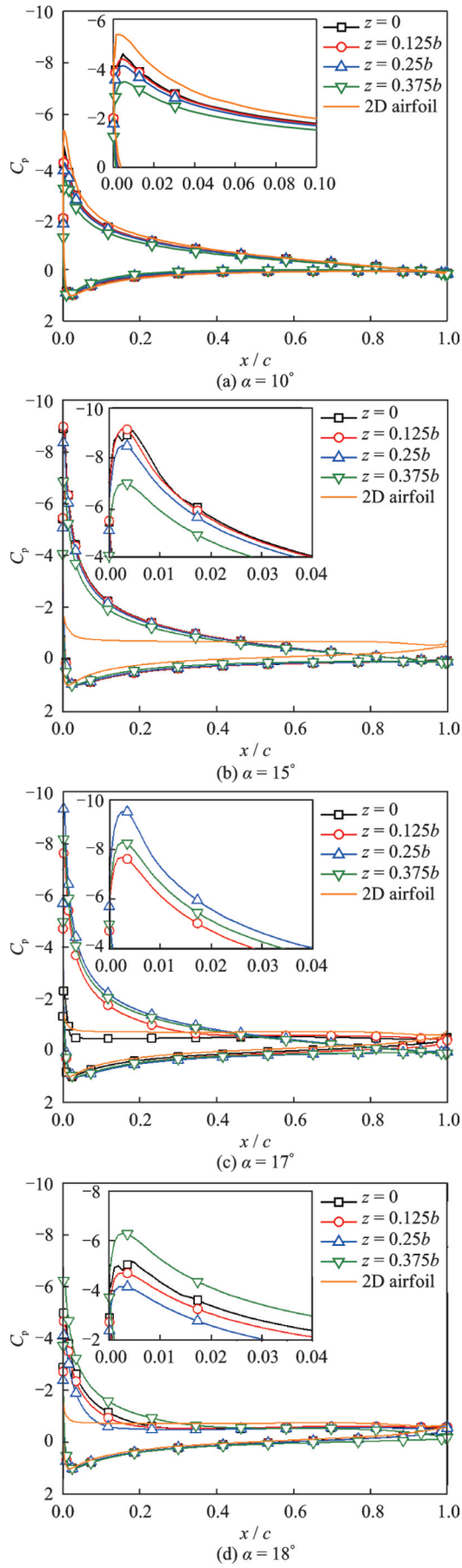

Fig.11 Comparisons of pressure coefficients of different spanwise sections

presented. At $\alpha = 10^\circ$, flow remains attached on both the wing and airfoil surfaces. The suction peaks of the wing sections are lower than those of the 2D airfoil. Additionally, as the wing section approaches the wing tip, the suction peak drops. This can be attributed to the increased strength of the downwash effects. As the AoA is increased to 15°, a collapse of the suction peak is observed on the 2D airfoil. The pressure coefficient remains nearly constant over the upper surface, indicating significant flow separation. In contrast, the suction peaks of the wing are higher compared to an AoA of 10°, revealing the flow still attaches to the wing surface. When α is increased from 15° to 17°, an abrupt drop in the suction peak is observed in the middle section ($z = 0$), indicating significant flow separation. The flow separation also affects the section at $z = 0.125b$, leading to a reduced suction peak compared to $\alpha = 15^\circ$. In the outer region ($z \geqslant 0.25b$), the flow still attaches to the surface. At $\alpha = 18^\circ$, flow separation impacts all four wing sections.

2.3 Dynamic characteristics

The aerodynamic characteristics of the pitching, finite wing are computed at a Mach number of 0.283. A sinusoidal pitching motion is considered with the reduced frequency $k = 0.151$, mean angle $\alpha_m = 14.91^\circ$ and pitching amplitude $\alpha_a = 9.88^\circ$. The solver runs for four cycles with 800 time steps in each cycle, resulting in a nondimensional time step of $\Delta t' = 0.026$. Fig.12 shows the aerodynamic force coefficients of the finite wing during one pitching cycle. The experimental[38] and numerical results of the 2D airfoil are also included in Fig.12. In the

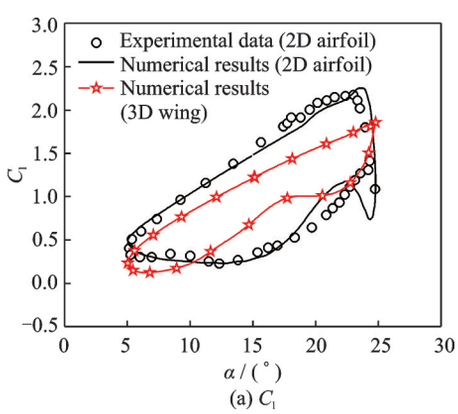

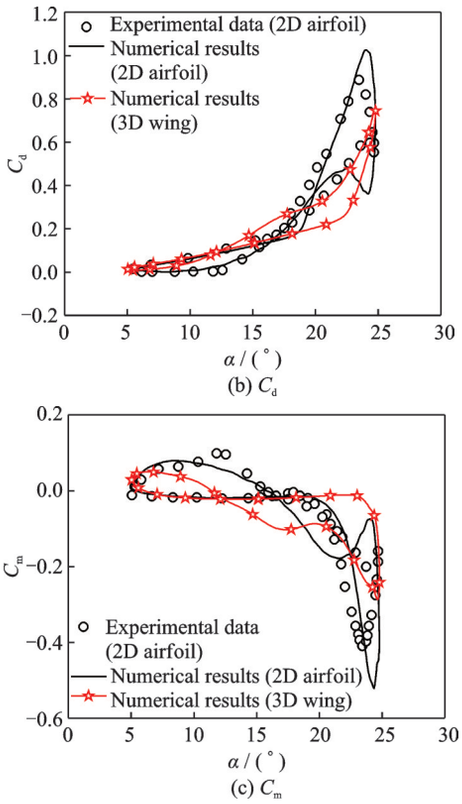

Fig.12 Comparisons of force coefficients of 2D airfoil and finite wing

pitch-up circle, the finite wing generates a decreased lift and exhibits a smaller lift slope in comparison to the 2D airfoil. Both the 2D airfoil and finite wing encounter dynamic stall, with the latter exhibiting a lighter feature. Moreover, the finite wing delays the lift stall and drag and moment divergence to a higher AoA.

Fig.13 illustrates the progression of the vortex structure during one pitching cycle of the finite wing. When the angle of attack reaches its maximum value of 24.79°, a DSV is already present on the upper surface of the wing. At this point, the 2D airfoil experiences a sudden decrease in lift (shown in Fig.13(a)), indicating the shedding of the DSV from the airfoil surface. As the finite wing pitches down, the DSV convects downstream (shown in Fig.13(b)). The DSV is fairly homogeneous in the spanwise direction, with the exception of the tip region. Subsequently, the DSV transforms into an Ω-type vortex with legs that are approximately perpendicular to the wing surface as the wing continues to pitch down, as demonstrated in Figs.13(c,d). At later stages, the Ω-type vortex undergoes vortex re-

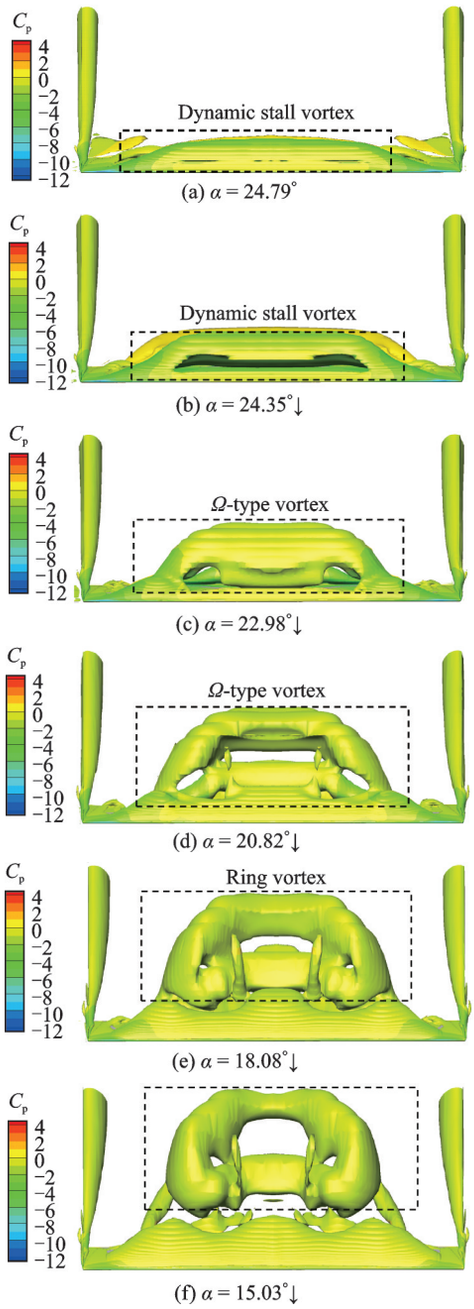

Fig.13 Iso-surface of Q colored by pressure coefficient for the finite wing at different angles in one pitching cycle

connection near the centerline of the wing, resulting in the formation of a ring-like vortical structure, as depicted in Figs.13(e, f). Eventually, this vortex ring is shed into the wake. The evolution of the DSV into an Ω-type and ring vortical structures observed in this study bears similarities to the flow phenomena found in the computations performed in Ref.[34]. The evolution of the vortex structure for the pitching wing significantly differs from the 2D

airfoil and exhibits highly 3D features.

Fig.14 displays the comparisons of force coefficients of different spanwise sections. During the pitching up circle, the lift slope gets smaller as the spanwise location approaches to the wing tip. Each cross-section demonstrates distinct dynamic stall characteristics. The cross-sections closer to the center experience an earlier onset of lift stall, drag, and moment divergence with a deep stall regime. Conversely, the cross-sections closer to the wing tip encounter a delayed occurrence of these phenomena, characterized by a light stall regime or no stall. The variation in dynamic stall behavior across the spanwise sections is primarily attributed to the different downwash effects induced by the wing tip vortex.

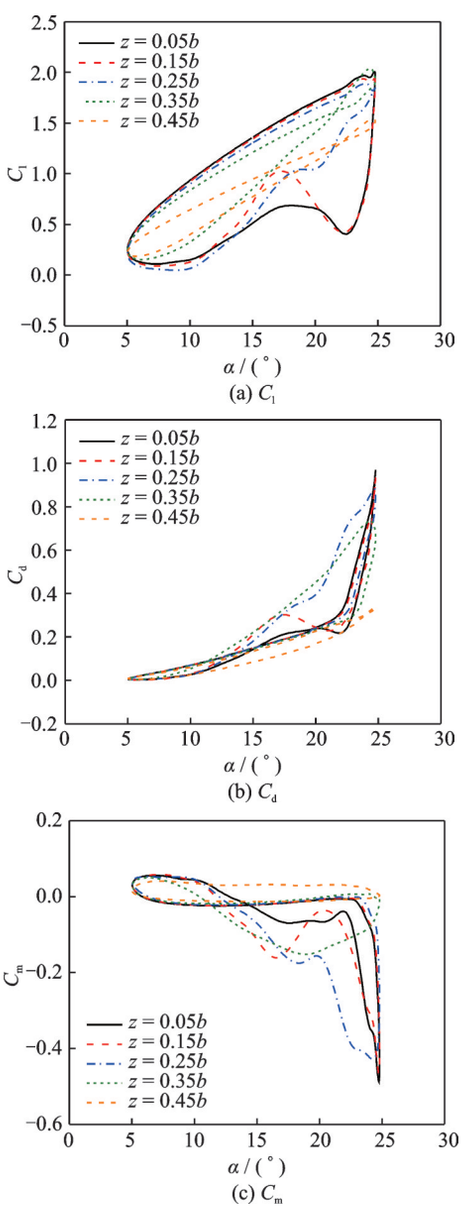

Fig.14 Comparisons of force coefficients of different spanwise sections

2.4 Aerodynamic damping

For helicopter rotor, torsional stability is tightly associated with aerodynamic damping. If the damping is negative, this would tend to promote stall flutter. The cycle-averaged aerodynamic damping coefficient, Ξ_{cycle} is defined as[39]

$$\Xi_{\text{cycle}} = -\frac{1}{\pi\alpha_a^2}\oint C_m \, d\alpha \tag{5}$$

where α_a denotes the pitching amplitude. The damping is positive when it corresponds to a counterclockwise loop in the C_m versus α curve.

A time-resolved aerodynamic damping coefficient $\Xi(t)$ is defined in Ref.[40].

$$\Xi(t) = -\frac{1}{\alpha_a}(\tilde{C}_m \cos\omega t - C_m \sin\omega t) = -\frac{\sqrt{C_m^2 + \tilde{C}_m^2}}{\alpha_a}\sin\left(\arctan\left(\frac{\tilde{C}_m}{C_m}\right) - \omega t\right) \tag{6}$$

where $\tilde{C}_m$ is obtained using the integral Hilbert transform of C_m.

Fig. 15 illustrates the pitching moment coefficient of the 2D airfoil and 3D wing in a pitch cycle. As can be seen in the figure, clockwise loops in the moment coefficient indicate negative damping, while counterclockwise loops suggest positive damping. Notably, the 3D wing, which exhibits a light stall regime, has a tendency to generate unstable aerodynamic loads. Additionally, Fig.16 reveals that the 2D airfoil produces positive cycle-averaged damping, whereas the 3D wing produces negative cycle-averaged damping. The comparison of time-re-

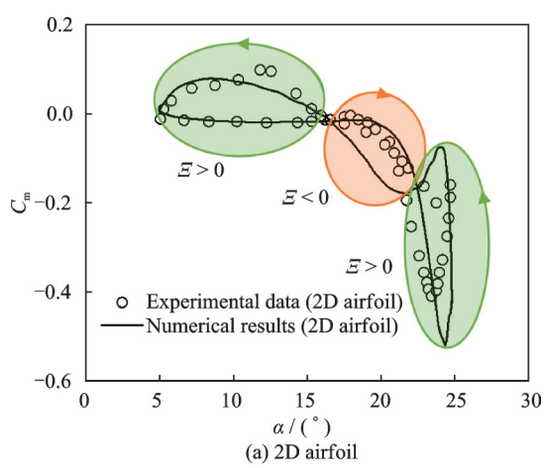

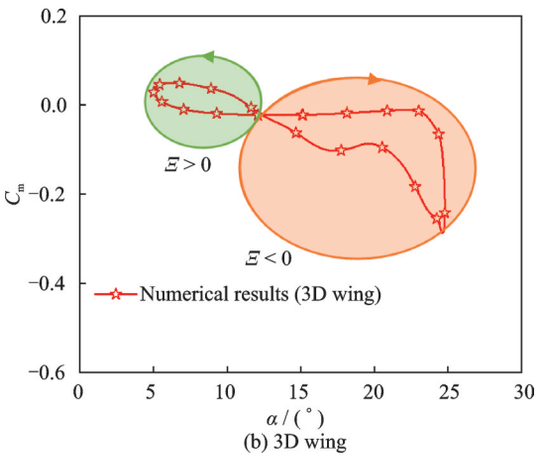

Fig.15 Aerodynamic damping from pitching moment

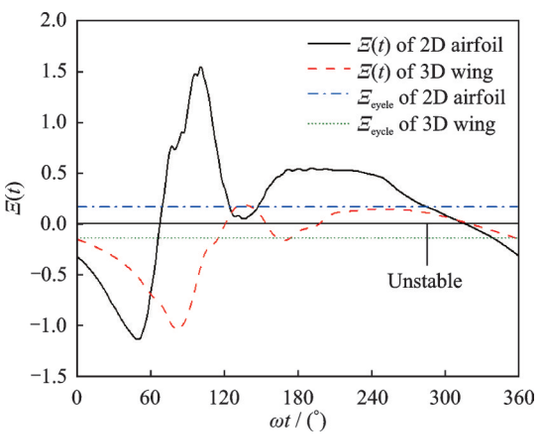

Fig.16 Comparisons of aerodynamic damping between 2D airfoil and 3D wing

solved damping between the 2D airfoil and 3D wing is presented in Fig.16. In particular, the finite wing demonstrates negative damping during a large phase range of 0° to 120°, in contrast to the airfoil's range of 0° to 70°, indicating a higher instability for the finite wing.

Fig.17 shows the variations of cycle-averaged damping with spanwise locations of the finite wing. It is illustrated that the inner section of the wing primarily generates negative damping, while positive damping is only observed within a small range near the tip. As the spanwise position moves from the middle towards the wing tip, a trend of initially increasing and then decreasing negative damping values is observed. This phenomenon is closely related to the wing's stall regime. The midsection of the wing, being relatively distant from the wing tip vortex, experiences a smaller downwash effect. Consequently, during pitch oscillation, a deep stall occurs, resulting in negative damping. As the spanwise position approaches the ends, the downwash effect on the section profile gradually intensifies, transitioning the deep stall into a light stall and yielding a larger negative damping. When the spanwise position further approaches the wing tip, the section profile experiences a strong downwash effect. This helps to alleviate dynamic stall, leading to a positive damping.

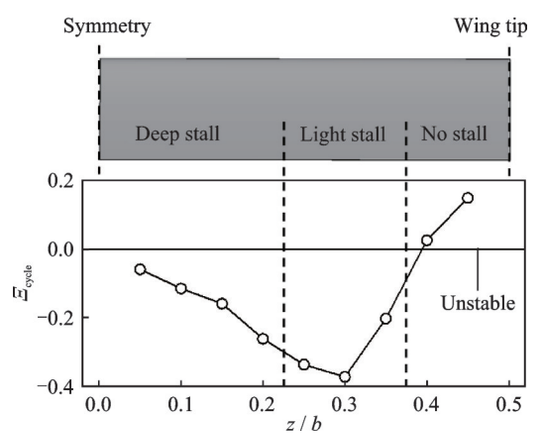

Fig.17 Variations of cycle-averaged damping with spanwise locations of the finite wing

3 Conclusions

The aerodynamic characteristics of a finite wing are computed and analyzed utilizing the URANS method. The findings are concluded as:

(1) Good agreements are achieved between the numerical and experimental results, indicating that the present CFD method can effectively and accurately simulate the dynamic stall characteristics of finite wings.

(2) For static cases, the wing reduces the lift slope and delays the stall to a higher AoA due to the downwash effects induced by the wing tip vortices. The flow separation starts near the middle section and spreads to both ends of the wing, forming several arch-type vortices.

(3) For dynamic cases, the aerodynamic forces of the wing resemble a light stall with reduced lift slope and delayed stall angle. The DSV exhibits relative uniformity in the spanwise direction, except in the tip region. As it convects along the surface, the DSV evolves into an Ω-type vortex before ultimately detaching from the wing in the form of a ring

structure. Due to the variances in downwash effects caused by the wing tip vortex, the cross-sections located in closer proximity to the wing tip undergo a light stall or no stall, while the cross-sections closer to the center encounter a deep stall.

(4) Compared with a 2D airfoil, the finite wing mitigates dynamic stall and experiences a light stall. However, the finite wing produces negative cycle-averaged and time-resolved damping over a larger range of phase compared to a 2D airfoil. The inboard sections of the wing primarily generate negative damping, particularly in sections that encounter a light stall.

References

[1] LEISHMAN J G. Principles of helicopter aerodynamics[M]. 2nd ed. Cambridge: Cambridge University Press, 2006.

[2] VISBAL M R, GARMANN D J. Dynamic stall of a finite-aspect-ratio wing[J]. AIAA Journal, 2019, 57(3): 962-977.

[3] CARR L W, CHANDRASEKHARA M S. A study of compressibility effects on dynamic stall of rapidly pitching airfoils[J]. Computer Physics Communications, 1991, 65(1/2/3): 62-68.

[4] FUNG K Y, CARR L W. Effects of compressibility on dynamic stall[J]. AIAA Journal, 1991, 29(2): 306-308.

[5] CARR L W, CHANDRASEKHARA M S. Compressibility effects on dynamic stall[J]. Progress in Aerospace Sciences, 1996, 32(6): 523-573.

[6] CHOUDHURI P G, KNIGHT D D. Effects of compressibility, pitch rate, and Reynolds number on unsteady incipient leading-edge boundary layer separation over a pitching airfoil[J]. Journal of Fluid Mechanics, 1996, 308: 195-217.

[7] SANGWAN J, SENGUPTA T K, SUCHANDRA P. Investigation of compressibility effects on dynamic stall of pitching airfoil[J]. Physics of Fluids, 2017, 29(7): 076104.

[8] KIM T, KIM S, LIM J, JEE S. Numerical investigation of compressibility effect on dynamic stall[J]. Aerospace Science and Technology, 2020, 105: 105918.

[9] BENTON S I, VISBAL M R. Effects of compressibility on dynamic-stall onset using large-eddy simulation[J]. AIAA Journal, 2020, 58(3): 1194-1205.

[10] NOONAN K W, BINGHAM G J. Aerodynamic characteristics of three helicopter rotor airfoil sections at Reynolds number from model scale to full scale at Mach numbers from 0.35 to 0.90: NASA-TP-1701[R]. [S.l.]: NASA, 1980.

[11] BAIK Y S, RAUSCH J M, BERNAL L P. Experimental investigation of pitching and plunging airfoils at Reynolds number between 1×10^4 and 6×10^4[C]// Proceedings of the 39th AIAA Fluid Dynamics Conference. San Antonio, Texas: AIAA, 2009.

[12] ZHU Wenbo, BONS J P, GREGORY J W. Reynolds scaling effects on dynamic stall of VR-7 and VR-12 airfoils[C]//Proceedings of the AIAA Scitech 2019 Forum. San Diego, California: AIAA, 2019.

[13] MCCROSKEY W J. The phenomenon of dynamic stall: NASA TM-81264[R]. [S.l.]: NASA, 1981.

[14] SHARMA A, VISBAL M. Numerical investigation of the effect of airfoil thickness on onset of dynamic stall[J]. Journal of Fluid Mechanics, 2019, 870: 870-900.

[15] SHUM J G, LEE S. Effect of Airfoil design parameters on deep dynamic stall under pitching motion[C]// Proceedings of the AIAA SCITECH 2023 Forum. National Harbor, MD: AIAA, 2023.

[16] MCCROSKEY W J, CARR L W, MCALISTER K W. Dynamic stall experiments on oscillating airfoils[J]. AIAA Journal, 1976, 14(1): 57-63.

[17] PIZIALI R A. 2-D and 3-D oscillating wing aerodynamics for a range of angles of attack including stall: NASA TM-4632[R]. [S.l.]: NASA, 1994.

[18] SCHRECK S J, HELIN H E. Unsteady vortex dynamics and surface pressure topologies on a finite pitching wing[J]. Journal of Aircraft, 1994, 31(4): 899-907.

[19] TANG D M, DOWELL E H. Experimental investigation of three-dimensional dynamic stall model oscillating in pitch[J]. Journal of Aircraft, 1995, 32(5): 1062-1071.

[20] COTON F N, GALBRAITH R A M. An experimental study of dynamic stall on a finite wing[J]. Aeronautical Journal, 1999, 103(1023): 229-236.

[21] BERTON E, ALLAIN C, FAVIER D, et al. Experimental methods for subsonic flow measurements[C]// Proceedings of the Progress in Computational Flow-Structure Interaction. New York: Springer-Verlag, 2003.

[22] BERTON E, ALLAIN C, FAVIER D, et al. Database for steady and unsteady, 2D and 3D flow[C]// Proceedings of Progress in Computational Flow-Structure Interaction. New York: Springer-Verlag, 2003.

[23] PAPE A L, PAILHAS G, DAVID F, et al. Extensive wind tunnel tests measurements of dynamic stall

phenomenon for the OA209 airfoil including 3D effects[C]//Proceedings of the 33rd European Rotorcraft Forum. Kazan, Russia:[s.n.], 2007.

[24] MERZ C B, WOLF C C, RICHTER K, et al. Experimental investigation of dynamic stall on a pitching rotor blade tip[C]//Proceedings of New Results in Numerical and Experimental Fluid Mechanics X. Munich, Germany:[s.n.],2017.

[25] EKATERINARIS J A. Numerical investigation of dynamic stall of an oscillating wing[J]. AIAA Journal, 1995, 33(10): 1803-1808.

[26] MORGAN P E, VISBAL M R. Simulation of unsteady three-dimensional separation on a pitching wing[C]//Proceedings of the 15th AIAA Computational Fluid Dynamics Conference. Anaheim, CA: AIAA, 2001.

[27] SPENTZOS A, BARAKOS G, BADCOCK K, et al. Investigation of three-dimensional dynamic stall using computational fluid dynamics[J]. AIAA Journal, 2005, 43(5): 1023-1033.

[28] SPENTZOS A, BARAKOS G N, BADCOCK K J, et al. Computational fluid dynamics study of three-dimensional, dynamic stall of various planform shapes[J]. Journal of Aircraft, 2007, 44(4): 1118-1128.

[29] MOHAMED K, NADARAJAH S, PARASCHIVOIU M. Detached-eddy simulation of a wing tip vortex at dynamic stall conditions[J]. Journal of Aircraft, 2009, 46(4): 1302-1313.

[30] COSTES M, RICHEZ F, LE PAPE A, et al. Numerical investigation of three-dimensional effects during dynamic stall[J]. Aerospace Science and Technology, 2015, 47: 216-237.

[31] KAUFMANN K, COSTES M, RICHEZ F, et al. Numerical investigation of three-dimensional static and dynamic stall on a finite wing[J]. Journal of the American Helicopter Society, 2015, 60(3): 032004.

[32] JAIN R, LE PAPE A, GRUBB A, et al. High-resolution computational fluid dynamics predictions for the static and dynamic stall of a finite-span OA209 wing[J]. Journal of Fluids and Structures, 2018, 78: 126-145.

[33] KAUFMANN K, MERZ C B, GARDNER A D. Dynamic stall simulations on a pitching finite wing[J]. Journal of Aircraft, 2017, 54(4): 1303-1316.

[34] VISBAL M R, GARMANN D J. Effect of sweep on dynamic stall of a pitching finite-aspect-ratio wing[J]. AIAA Journal, 2019, 57(8): 3274-3289.

[35] WANG Qing, ZHAO Qijun. Numerical study on dynamic-stall characteristics of finite wing and rotor[J]. Applied Sciences, 2019,9(3): 600.

[36] ZHAO Qijun, ZHAO Guoqing, WANG Bo, et al. Robust Navier-Stokes method for predicting unsteady flowfield and aerodynamic characteristics of helicopter rotor[J]. Chinese Journal of Aeronautics, 2018, 31(2): 214-224.

[37] MCCROSKEY W J, MCALISTER K W, CARR L W,et al. An experimental study of dynamic stall on advanced airfoil sections, Volume 1: Summary of the experiment: NASA-TM-84245[R]. [S. l.] : NASA, 1982.

[38] MCALISTER K W, PUCCI S L, MCCROSKEY W J,et al. An experimental study of dynamic stall on advanced airfoil sections, Volume 2: Pressure and force data:NASA-TM-84245[R]. [S.l.]:NASA, 1982.

[39] CARTA F O. An analysis of the stall flutter instability of helicopter rotor blades[J]. Journal of the American Helicopter Society, 1967, 12(4): 1-18.

[40] BOWLES P O, CORKE T C, COLEMAN D G, et al. Improved understanding of aerodynamic damping through the Hilbert transform[J]. AIAA Journal, 2014, 52(11): 2384-2394.

Acknowledgements This work was supported by the National Natural Science Foundation of China (No.12072156), the National Key Laboratory Foundation of China (No. 61422202103), and the Priority Academic Program Development of Jiangsu Higher Education Institutions (PAPD).

Authors Ms. **JING Simeng** is a Ph.D. candidate at Nanjing University of Aeronautics and Astronautics (NUAA). Her research domain indudes CFD, dynamic stall, and the design of rotor.

Dr. **ZHAO Guoqing** received his Ph.D. degree from NUAA in 2015. His research interests are helicopter aerodynamics, CFD, active flow control, and the design of rotor, etc.

Author contributions Ms. **JING Simeng** designed the study, conducted the wind tunnel tests, performed computations and analysis, and wrote the manuscript. Dr. **CAO Chenkai** and Mr. **GAO Yuan** contributed to a portion of the wind tunnel tests and computations. Prof. **ZHAO Qijun** and Dr. **ZHAO Guoqing** contributed to the discussion and provided background information for the study. All authors commented on the manuscript draft and approved the submission.

Competing interests The authors declare no competing interests.

(Production Editor: SUN Jing)

有限翼展机翼动态失速特性的数值研究

井思梦，曹宸恺，高　远，招启军，赵国庆

（南京航空航天大学直升机动力学全国重点实验室，南京 210016，中国）

摘要：研究了展弦比为8的有限翼展机翼的动态失速特性，以深入了解三维效应对流场结构、气动特性和俯仰阻尼的影响。首先，构建了计算流体动力学方法来模拟机翼的气动特性，采用有限体积法求解URANS方程，通过k-ω（Shear stress transport，SST）两方程湍流模型来考虑黏性效应。然后，采用上述CFD方法模拟了静态平直机翼和俯仰振荡尖削机翼的气动特性，数值结果与试验数据之间良好的一致性验证了CFD方法的有效性和准确性。最后，计算分析了有限翼展机翼在静态及动态状态下的气动特性。研究表明：无论是静态失速还是动态失速过程，机翼流场中均出现了显著的三维流场结构，包括翼尖涡、弓形涡、Ω涡和环形涡等，这些现象导致机翼的气动特性显著区别于二维翼型，具体表现为：附着流阶段升力线斜率减小、失速角增大以及失速更为平缓；气流分离最先出现在机翼中部，随后逐渐向两端扩展；至于气动阻尼特性，不稳定载荷主要由机翼内段产生；此外，与深度失速的翼段相比，轻度失速的翼段更易产生负阻尼。

关键词：有限翼展机翼；动态失速；气动阻尼；三维效应